Effects of carbonate distribution pattern on the mechanical behaviour of bio-cemented sands

A DEM study

Zhang, Aoxi; Dieudonné, Anne Catherine

DOI
10.1016/j.compgeo.2022.105152

Publication date
2023

Document Version
Final published version

Published in
Computers and Geotechnics

Citation (APA)
Zhang, A., & Dieudonné, A. C. (2023). Effects of carbonate distribution pattern on the mechanical behaviour of bio-cemented sands: A DEM study. *Computers and Geotechnics*, *154*, Article 105152. https://doi.org/10.1016/j.compgeo.2022.105152

Computers and Geotechnics 154 (2023) 105152

Contents lists available at ScienceDirect

Computers and Geotechnics

journal homepage: www.elsevier.com/locate/compgeo

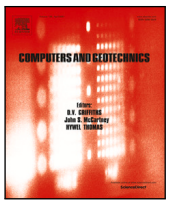

Research paper

Effects of carbonate distribution pattern on the mechanical behaviour of bio-cemented sands: A DEM study

Aoxi Zhang, Anne-Catherine Dieudonné *

Geo-Engineering Section, Faculty of Civil Engineering and Geosciences, Delft University of Technology, Delft, The Netherlands

ARTICLE INFO

Keywords:
Bio-cemented soils
Discrete element method
Microstructure
Shear strength

ABSTRACT

Microbially induced carbonate precipitation is a promising ground improvement technique which can enhance the mechanical properties of soils through the precipitation of calcium carbonate. Experimental evidences indicate that the precipitated carbonate can display different distribution patterns. Crystals can develop at grain–grain contacts (contact cementing), connect soil grains that were initially not in contact with each other (bridging), precipitate on the grain surface (coating), or fill in the void space (pore filling). This paper investigates the role of the aforementioned distribution patterns on the mechanical behaviour of lightly bio-cemented soil samples using discrete element modelling. Bio-cemented samples with different distribution patterns and carbonate contents are built, and a series of drained triaxial compression simulations are carried out at different confining pressures. The results show that cementation in the form of bridging and contact cementing leads to obvious improvement in stiffness, strength and dilatancy. In contrast, cementation in the form of coating contributes only slightly to mechanical improvement, and pore filling exhibits negligible influence on the mechanical response of the material. The findings suggest that, to gain strength improvement in the most effective way, treatments should be tailored to precipitate calcium carbonate crystals in the form of bridging.

1. Introduction

In recent decades, bio-mediated soil improvement methods have attracted significant attention as ecological alternatives to invasive, carbon-intensive stabilisation techniques. These methods, which include microbially induced carbonate precipitation (MICP) and enzyme induced carbonate precipitation (EICP), use biogeochemical processes to drive carbonate precipitation and cement soil grains, thereby improving the material mechanical performance. Possible applications span ground improvement (van Paassen et al., 2010; Zeng et al., 2021), liquefaction mitigation (Xiao et al., 2018; Darby et al., 2019), protection against soil erosion (Salifu et al., 2016; Jiang and Soga, 2017; Shahin et al., 2020; Clarà Saracho et al., 2021a), dust control (Hamdan and Kavazanjian, 2016), and heavy metal removal (Li et al., 2013, 2016), among others. Soils treated through MICP or EICP exhibit an increase in stiffness, strength and dilatancy (see van Paassen et al., 2010; Al Qabany and Soga, 2013; Montoya and DeJong, 2013; Chu et al., 2014; Cheng et al., 2016; Hoang et al., 2018; Liu et al., 2019; Terzis and Laloui, 2019a; Tang et al., 2020; Nafisi et al., 2020; Xiao et al., 2021b, among others), yet often with variable magnitudes, even at equal calcium carbonate contents. Several reasons can explain this variability: differences in sizes and distribution patterns of the precipitated minerals (DeJong et al., 2010; Lin et al., 2015; Mujah et al., 2017; Wang et al., 2022), precipitation of different polymorphs of calcium carbonate (i.e. vaterite, aragonite or calcite) or of amorphous calcium carbonate (Van Paassen, 2009; Terzis and Laloui, 2019b), and inhomogeneity of the treated samples (Xiao et al., 2021b; Zhang and Dieudonné, 2023). In particular, four typical distribution patterns of bio-treated sands can be identified (Fig. 1) using scanning electron microscopy (SEM) (Van Paassen, 2009; Al Qabany and Soga, 2013; Feng and Montoya, 2015; Lin et al., 2015; Hoang et al., 2018; Mahawish et al., 2018; Cheng et al., 2019; Xiao et al., 2021a) or micro-CT scanning (Dadda et al., 2017; Terzis and Laloui, 2018; Clarà Saracho et al., 2021b), namely contact cementing, bridging, grain coating and pore filling. Contact cementing and bridging lead to the formation of carbonate bonds between sand grains. In the case of contact cementing, the cemented sand grains were already in contact with each other prior to cementation, while bridging corresponds to the formation of carbonate bonds between sand grains which were initially not in contact. Several factors are known to affect the distribution pattern of calcium carbonate and can be partly controlled. These include the treatment conditions, such as the concentration of the injected solutions (Okwadha and Li, 2010; Al Qabany et al., 2012), the injection approach (Cheng et al., 2019;

* Corresponding author.
E-mail address: A.A.M.Dieudonne@tudelft.nl (A.-C. Dieudonné).

https://doi.org/10.1016/j.compgeo.2022.105152
Received 30 November 2021; Received in revised form 28 October 2022; Accepted 21 November 2022
Available online 17 December 2022

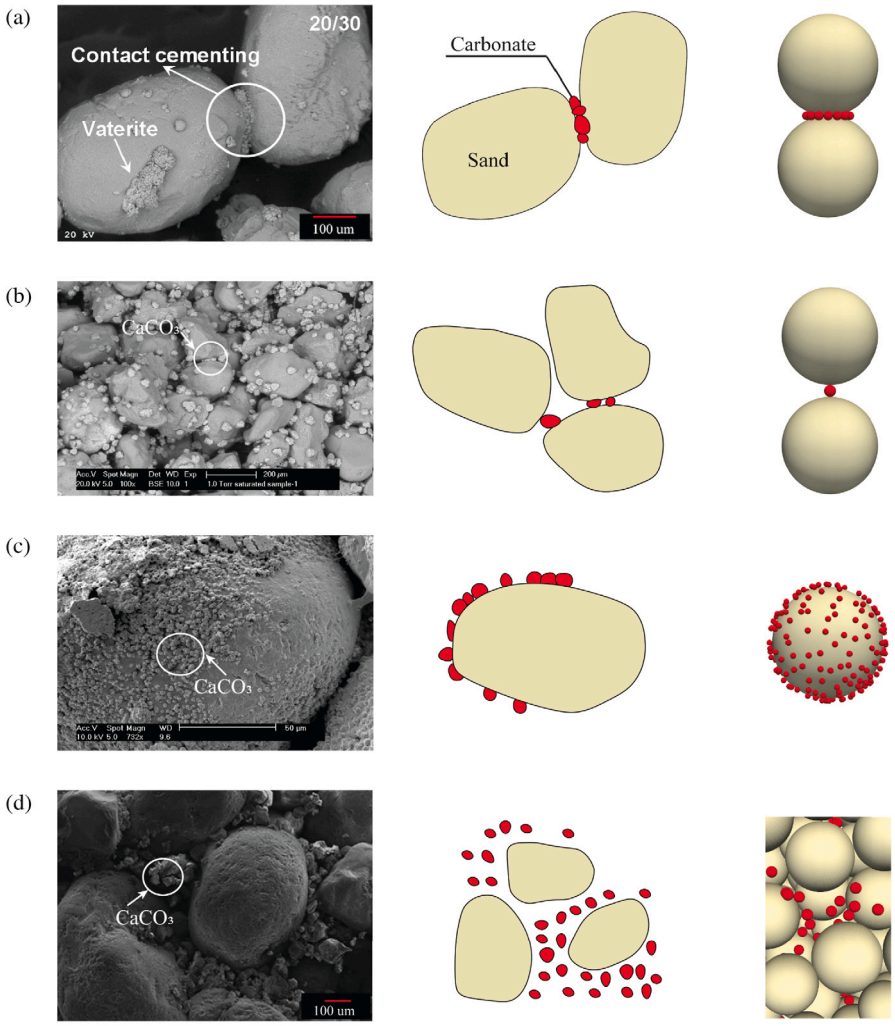

Fig. 1. Microstructure (left), conceptualisation (middle) and DEM idealisation (right) of the four distribution patterns. (a) Contact cementing (SEM image from Lin et al. (2015)), (b) bridging (SEM image from Van Paassen (2009)), (c) grain coating (SEM image from Cheng et al. (2016)) and (d) pore filling (SEM image from Wu et al. (2021)).

Xiao et al., 2021b), the use of additional ingredients such as powdered milk (Almajed et al., 2019), the nature of the soil (Lin et al., 2015), its degree of saturation (Cheng et al., 2013), temperature (Cheng et al., 2016) and the solution pH (Okwadha and Li, 2010). Note that the distribution of calcium carbonate in bio-cemented soils significantly differs from that of other artificially cemented soils, in which water-insoluble hydrates (e.g. Portland cement) occupy most of the pore space, typically forming a denser microstructure than bio-cemented soils (Cheng et al., 2013; Yu et al., 2019). Contact cementing, bridging, grain coating and pore filling are expected to contribute differently to the mechanical performance of bio-cemented soils. However, in practice, bio-cemented soil samples exhibit a combination of distribution patterns, so that the effects of individual distributions cannot be easily assessed experimentally. This paper sheds the light on the role of the carbonate distribution patterns on the mechanical behaviour of bio-cemented sands using discrete element modelling (DEM).

Two approaches have been used to model cemented soils using the discrete element method. The most commonly adopted approach consists in simulating the effects of cementation by introducing virtual bonds (such as parallel bonds) between soil grains (Utili and Nova, 2008; Shen et al., 2016; Feng et al., 2017; Yang et al., 2019). This method implicitly assumes contact cementing between grains. Overall, the approach is able to capture some features of cemented soils, such as the increase in peak strength and dilatancy, but may lead to an underestimation of the ultimate strength as the bonds disappear after breakage (Feng et al., 2017). Furthermore, the mass content of carbonate is only considered implicitly in the model. An alternative modelling approach consists in representing the cement agents using real particles (Wang and Leung, 2008a,b; Evans et al., 2014; Li et al., 2017; Khoubani, 2018). In this case, different distribution patterns and mass contents of calcium carbonate can be considered, leading to a better representation of the post-peak behaviour. The main drawback of this approach is the computational cost associated with the increased number of particles.

In this paper, the latter DEM approach is adopted to investigate the role of the carbonate distribution patterns on the mechanical performance of lightly bio-cemented sands. Four types of bio-cemented samples are modelled such that each sample contains only one carbonate distribution pattern. The DEM samples are then subjected to drained triaxial compression under different confining pressures. The effects of the carbonate distribution pattern, confining pressure and carbonate content on the mechanical performance of bio-cemented sands are investigated. The role of the microstructure and bond breakage evolution on the macroscopic response is thoroughly analysed.

2. Discrete element model

2.1. Microstructure idealisation

In order to assess the role of the carbonate distribution pattern on the mechanical behaviour of cemented soils, idealised DEM samples

with a single distribution pattern are generated. Fig. 1 presents the idealised microstructures corresponding to the four types of carbonate distributions, namely contact cementing, bridging, grain coating and pore filling. Sand grains and carbonate particles are modelled using spheres. In the case of contact cementing (Fig. 1(a)), carbonate particles are located around sand–sand contacts, forming a cement chain. Carbonate particles of a given cement chain have the same size, and neighbouring carbonate particles are in contact with each other. Fig. 1(b) shows the bridging type of distribution, where one carbonate particle is used to represent the cement bridge. For grain coating, all carbonate particles bound to a given sand grain are assumed to have the same size and are randomly distributed at the surface of the sand grain (Fig. 1(c)). Finally, carbonate particles are randomly distributed in the pore space of the host sand in the case of pore filling (Fig. 1(d)). Note that, in the absence of gravity, these carbonate particles are initially not in contact with sand particles.

2.2. Inter-particle contact laws

The discrete element simulations are performed using the open-source platform YADE (Šmilauer et al., 2015). A cohesive–frictional contact model, based on the classical linear elastic–plastic law from Cundall and Strack (1979) and accounting for rolling and twisting resistance, is used. Details of this contact model can be found in Bourrier et al. (2013) and Šmilauer et al. (2015).

For two spheres of radii R_1 and R_2 in contact, the normal force $\vec{F}_n$, incremental shear force $\Delta\vec{F}_s$, incremental rolling moment $\Delta\vec{M}_r$ and incremental twisting moment $\Delta\vec{M}_{tw}$ are calculated as:

$$\vec{F}_n = k_n u_n \vec{n} \tag{1}$$

$$\Delta\vec{F}_s = -k_s \Delta\vec{u}_s \tag{2}$$

$$\Delta\vec{M}_r = -k_r \Delta\vec{\theta}_r \tag{3}$$

$$\Delta\vec{M}_{tw} = -k_{tw} \Delta\vec{\theta}_{tw} \tag{4}$$

where u_n is the relative normal displacement of the two spheres, $\vec{n}$ is the normal contact vector, $\Delta\vec{u}_s$ is the incremental tangential displacement, and $\Delta\vec{\theta}_r$ and $\Delta\vec{\theta}_{tw}$ are the relative rotations due to rolling and twisting respectively. k_n, k_s, k_r and k_{tw} are the contact normal stiffness, tangential stiffness, rolling stiffness and twisting stiffness respectively, which are given by:

$$k_n = \frac{2E_1R_1E_2R_2}{E_1R_1 + E_2R_2} \tag{5}$$

$$k_s = \nu k_n \tag{6}$$

$$k_r = \alpha_r R_1 R_2 k_s \tag{7}$$

$$k_{tw} = \alpha_{tw} R_1 R_2 k_s \tag{8}$$

where E_i $(i = 1, 2)$ is the modulus of elasticity of particle i, ν is the shearing stiffness coefficient, and α_r and α_{tw} are the rolling and twisting stiffness coefficients respectively.

The normal, shear, rolling and twisting resistances are equal to:

$$F_n^{max} = \sigma_{coh} \min(R_1, R_2)^2 \tag{9}$$

$$F_s^{max} = \|\vec{F}_n\| \tan\varphi_c' + \sigma_{coh} \min(R_1, R_2)^2 \tag{10}$$

$$M_r^{max} = \|\vec{F}_n\| \eta_r \min(R_1, R_2) \tag{11}$$

$$M_{tw}^{max} = \|\vec{F}_n\| \eta_{tw} \min(R_1, R_2) \tag{12}$$

where σ_{coh} is a cohesive strength parameter which controls the adhesion forces in the normal and tangential directions. φ_c' is the contact friction angle, and η_r and η_{tw} are the resistance coefficients of rolling and twisting, respectively. In general, an increase in the contact friction angle φ_c' leads to an increase in peak strength and dilatancy, but has limited influence on ultimate strength. On the other hand, an increase in the resistance coefficients η_r and η_{tw} results in an increase in both peak and ultimate strengths, as well as in dilatancy. Further discussion on the effects of the contact model parameters on the macroscopic response of granular assemblies is available in Aboul Hosn et al. (2017).

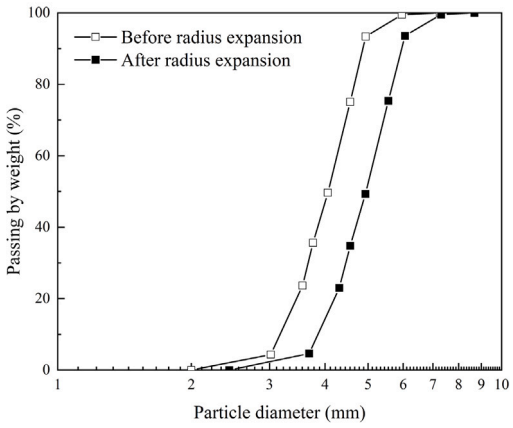

Fig. 2. Particle size distribution of the uncemented (host) sand before and after radius expansion.

Table 1
Ranges of carbonate particle size for bio-cemented sands displaying different distribution patterns. (unit: mm).

	Bridging	Contact cementing	Coating	Pore filling
Carbonate particle radii	0.3 – 0.86	0.12 – 0.37	0.18 – 0.65	0.42

2.3. Sample preparation and model parameters

Bio-cemented samples with different carbonate distribution patterns are generated from the same host uncemented sand. The procedure for preparing DEM samples of host sand and bio-cemented soil is as follows:

1. A sand packing containing 7000 sand particles is generated. The original particle size distribution can be found in Fig. 2. All the particles are randomly located inside a 7 cm × 7 cm × 14 cm box formed by six rigid walls. There is no contact between the particles at this stage.
2. The radius expansion method incorporated in YADE is used for isotropic compression. Accordingly, the radius of the sand particles is increased proportionally to their initial size until reaching a confining pressure of 100 kPa. The radius expansion is then turned off to fix the size of the particles, and the inter-particle friction angle is adjusted to reach a target porosity of 0.439. During this process, the rigid walls are controlled by a servomechanism to maintain the confining pressure. Once the target porosity is reached, the friction angle is set to the value which is used for the deviatoric loading stage. For samples tested under higher confining pressures (i.e. 200 kPa and 400 kPa), the confining pressure is further increased by moving the lateral walls. The particle size distribution of the host sand after radius expansion is shown in Fig. 2.
3. After the generation of the host sand sample at different confining pressures, an algorithm is used to introduce the carbonate particles at the designed positions and obtain the bio-cemented samples with the different distribution patterns. Bio-cemented samples with 3 different carbonate mass contents (mass of carbonate over total mass of the sample) are investigated in this study, namely 1%, 2% and 3%. Illustrations of the four types of bio-cemented samples are presented in Fig. 3. The size of particles of bio-cemented samples are summarised in Table 1. It should be noted that, for a given cemented sample, the size of the carbonate particles is not uniform, but belongs to a certain range, which varies slightly for the different distribution patterns.

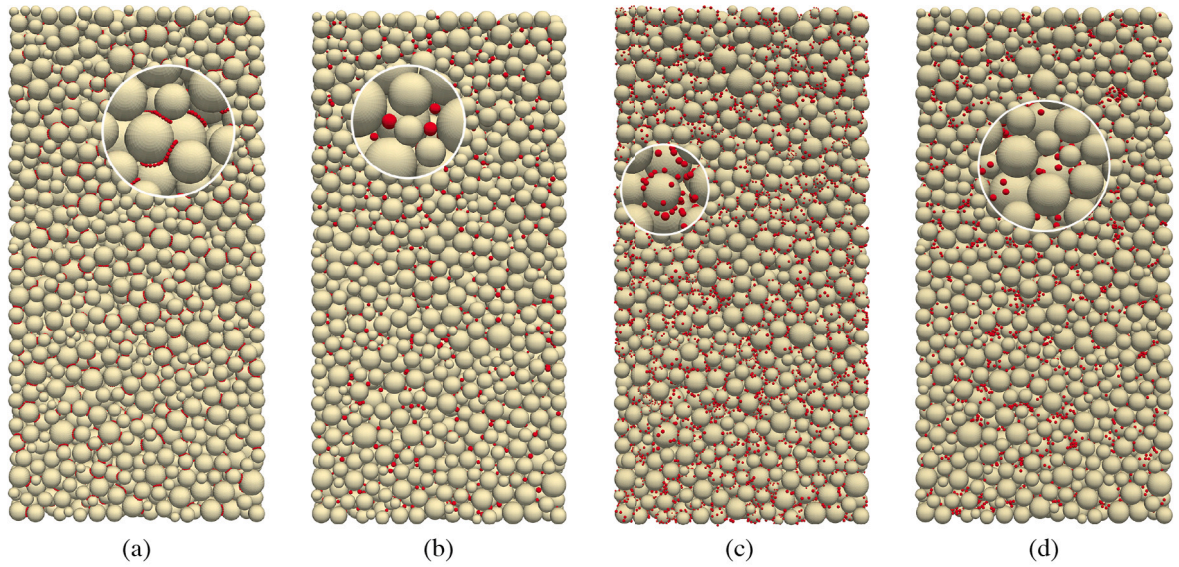

Fig. 3. DEM samples of idealised bio-cemented sands displaying different distribution patterns. (a) Contact cementing, (b) bridging, (c) grain coating, and (d) pore filling.

Table 2
Properties of the particles used in the DEM simulations.

Properties	Symbol	Unit	Sand	Carbonate
Density	ρ	kg/m^3	2650	2710
Young's modulus	E	MPa	200	180
Shearing stiffness coefficient	ν	–	0.3	0.3
Friction angle	φ_c'	°	19	19
Rolling stiffness coefficient	α_r	–	0.8	0.8
Twisting stiffness coefficient	α_{tw}	–	0.8	0.8
Rolling resistance coefficient	η_r	–	0.15	0.15
Twisting resistance coefficient	η_{tw}	–	0.15	0.15

The parameters used for the sand and carbonate particles are listed in Table 2. The parameters of the sand particles correspond to rough sand grains. The Young's modulus of quartz is around 97 GPa (Peng and Redfern, 2013), while the Young's modulus of calcite is around 88.2 GPa (Ekprasert et al., 2020). Accordingly, the Young's modulus of carbonate is assumed to be 0.9 times the Young's modulus of sand. The shearing stiffness coefficient (ν), friction angle (φ_c'), rolling and twisting stiffnesses (α_{r} and α_{tw}), and rolling and twisting resistances (η_{r} and η_{tw}) of carbonate particles are assumed to be the same as those of the sand particles given the lack of experimental data. In this study, the aforementioned parameters are maintained constant throughout the simulations, including after bond breakage. However, it should be noted that a recent study by Ren et al. (2021) suggested that the residual strength of cemented grains is slightly greater than the one of uncemented grains due to the formation of debris at the grain surface. Cohesion is only applied on initial sand–carbonate (S–C) and carbonate–carbonate (C–C) contacts and vanishes once a bond is broken. The cohesive strength of S–C contacts ($\sigma_{coh}^{\mathrm{S-C}}$) is set equal to 10 MPa. The cohesive strength of C–C contacts is assumed to be 5 times smaller than $\sigma_{coh}^{\mathrm{S-C}}$ as it has been observed by Montoya and Feng (2015) that failure tends to occur in the cement phase. Further insights into the micromechanics of cemented grains can be found from Ren et al. (2021), confirming the brittle nature of both tensile and shear failure.

The uncemented sample and idealised bio-cemented samples are subjected to drained triaxial loading. The deviatoric loading is conducted by a servomechanism which maintains a constant confining pressure on the four lateral walls. All walls are frictionless. The bottom wall is fixed while a constant strain rate is applied on the top wall. The strain rate is set as 1/s to speed up the simulations. The inertial number I is used to verify quasi-static conditions of the packing (Da Cruz et al., 2005; Rakhimzhanova et al., 2019; Jiang et al., 2019). It is defined as $I = \dot{\varepsilon}\bar{d}\sqrt{\rho/p'}$, where $\dot{\varepsilon}$ is the strain rate, $\bar{d}$ is the mean diameter of particles in the sample, ρ is the particle density and p' is the mean effective stress. The inertial number of uncemented sand is 7.16×10^{-4} for $p' = 100$ kPa, which is smaller than the value of 1×10^{-3} suggested by Da Cruz et al. (2005). The inertial number of bio-cemented samples is lower than that of uncemented sample as cemented samples have a much smaller mean particle diameter than uncemented sample. Consequently, quasi-static conditions are ensured for all simulations.

3. Results and discussion

In this section, the macroscopic stress–strain relationship and volumetric response of different packings are assessed. The results are analysed to investigate the effects of the carbonate distribution pattern, confining pressure and carbonate content on the macroscopic response of bio-cemented soils. Microscopic observations, focusing on the coordination number evolution and bond breakage behaviour, are then used to get further insights into the macroscopic response.

3.1. Macroscopic responses

3.1.1. Effects of the carbonate distribution pattern

The effects of the carbonate distribution pattern on the mechanical response of bio-cemented sands are highlighted in Fig. 4. It reveals that carbonates distributed in the patterns of bridging and contact cementing significantly affect the stiffness (denoted as E_{50} in Fig. 4(a)), strength and volumetric response of samples with 1% carbonate content. Coating results in a slight improvement of strength and dilatancy, while pore filling has negligible effects on the response of the material. The stress–strain responses, and in particular the yielding pattern, of contact cementing and bridging are fundamentally different. The sample with a bridging cementation exhibits a higher peak strength and relatively brittle yielding as compared to contact cemented samples, whose behaviour is associated with strain softening. This difference in mechanical response can be explained by different initial carbonate distribution patterns and different evolutions of the carbonate distribution upon shearing, which is further discussed based on microscopic observations in Section 3.2.

Fig. 4(b) shows that samples with cementation in the forms of bridging and contact cementating exhibit obvious dilatancy enhancement as a result of particles bonding. This enhancement in dilatancy of

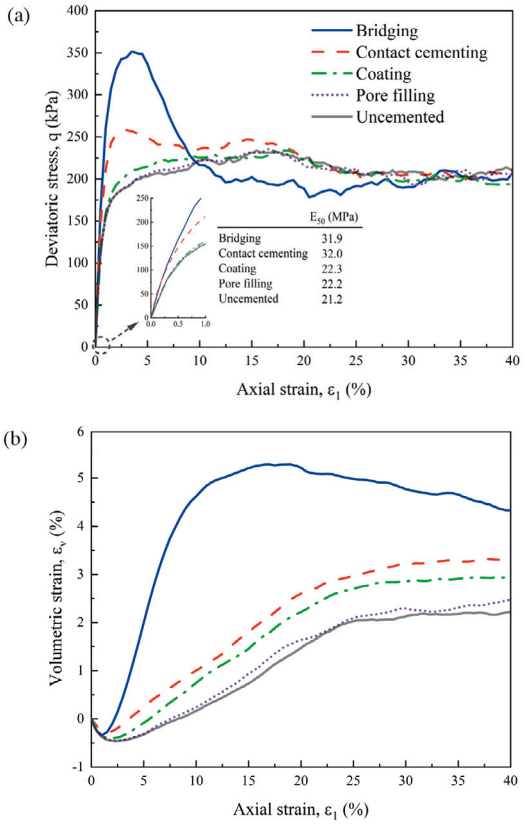

Fig. 4. Effects of the carbonate distribution pattern on the shear response of bio-cemented samples with 1% carbonate content and under a confining pressure of 100 kPa. (a) Stress–strain response and (b) volumetric response.

bio-cemented sands is generally observed in experimental studies (see Wang and Leung, 2008b; Nafisi et al., 2020; Wu et al., 2021, among others). The enhancement is attributed to the irregular particle clusters formed of sand grains and binders (Shen et al., 2016). These clusters lead to a more open soil structure and larger volumetric strain upon shearing as compared to the uncemented material. In addition, the unbroken clusters prevent the high void space from collapsing, thereby maintaining a high volumetric strain at large strain, as reported by Wang and Leung (2008b). Finally, the bio-cemented sample with coating pattern shows increase in dilatancy, which can be attributed to additional interlocking of particles upon shearing. This can be inferred from the evolution of coordination number of carbonate, which is discussed in Section 3.2.

3.1.2. Effects of the confining pressure

Fig. 5 shows the results of triaxial simulations on bio-cemented samples with 1% carbonate content at confining pressures of 200 kPa and 400 kPa. Qualitatively, the mechanical behaviour of each type of bio-cemented samples under 200 kPa and 400 kPa confinement is similar to the corresponding case at 100 kPa. On the other hand, the improvement in strength for bridging and contact cementing becomes negligible with respect to the effect of the increasing confining pressure. This finding is consistent with experimental observations from Feng and Montoya (2015) and Nafisi et al. (2020), in which lightly bio-cemented samples exhibit limited improvement in strength under a confining pressure of 400 kPa.

3.1.3. Effects of carbonate content

Cemented samples with carbonate contents up to 3% show similar mechanical behaviour as samples with a carbonate content of 1% in

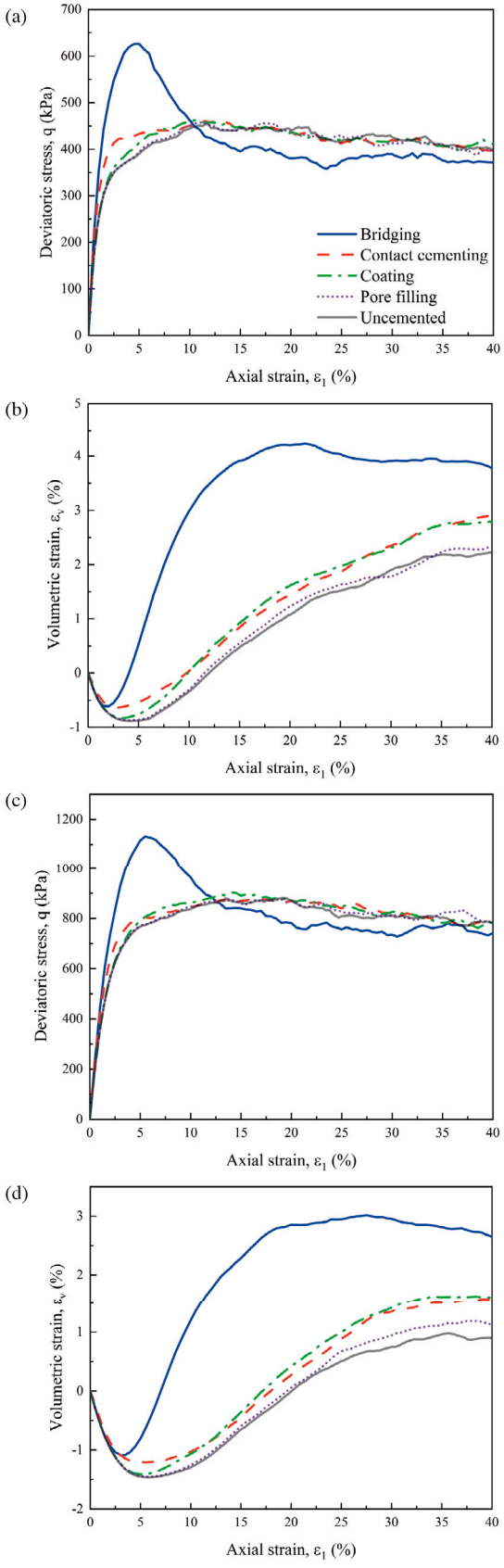

Fig. 5. Effects of the confining pressure on the mechanical response of bio-cemented samples with 1% carbonate content. (a) Stress–strain response and (b) volumetric response upon shearing under a confining pressure of 200 kPa. (c) Stress–strain response and (d) volumetric response upon shearing under a confining pressure of 400 kPa.

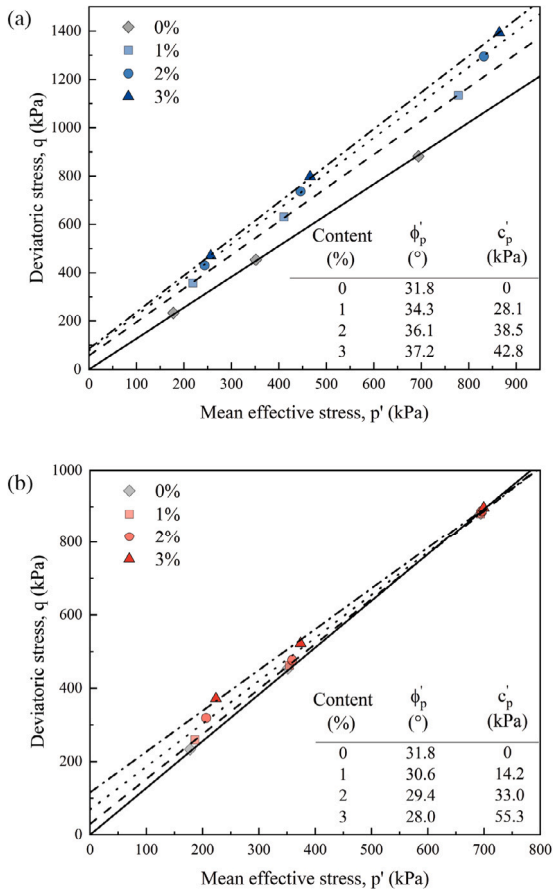

Fig. 6. Peak strength envelopes for different carbonate contents. (a) Bridging and (b) contact cementing.

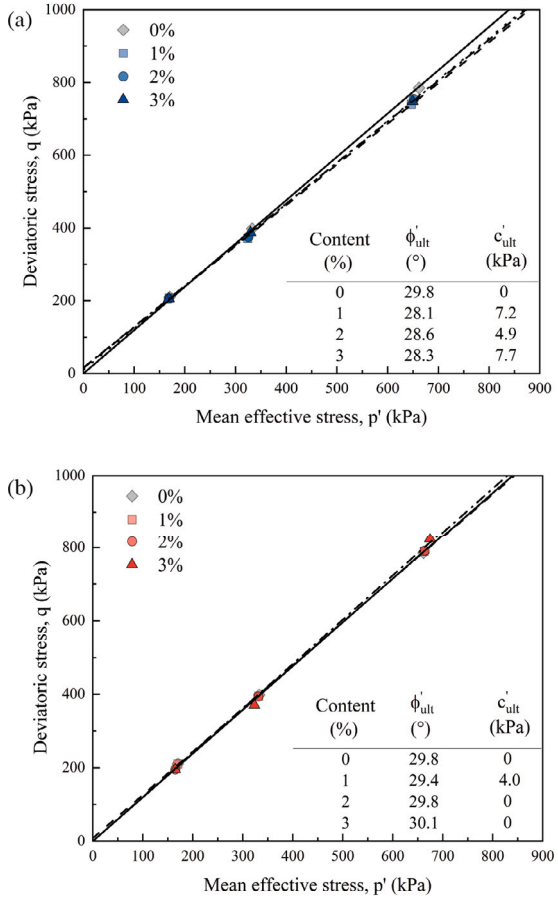

Fig. 7. Ultimate strength envelopes for different carbonate contents. (a) Bridging and (b) contact cementing.

general. Fig. 6 shows the strength envelopes at the peak and ultimate states (ε_1 = 40%), and their evolution with carbonate content, in the case of bridging and contact cementing samples. The effective friction angle (ϕ') and cohesion (c') at each state are derived using a linear Mohr–Coulomb criterion. Fig. 6 shows that a higher carbonate content leads to a higher peak strength in both bridging and contact cementing cases. Moreover, the increase in peak strength is associated with increases in both friction angle and cohesion in the case of bridging, while the increase in peak strength for contact cementing case mainly arises from an increase in cohesion rather than friction. The friction angles at the ultimate state of both bridging and contact cementing samples remain fairly constant with increasing carbonate content, as shown in Fig. 7. The relationship between carbonate content and improvement in cohesion is further elaborated in Fig. 8, from which a linear relationship can be inferred between carbonate content and peak cohesion. This finding is consistent with what has been reported by Wu et al. (2021). In addition, the increase in peak cohesion with increasing carbonate contents is higher for contact cementing than bridging pattern. The cohesion at the ultimate state is low, especially for contact cementing case. This can be attributed to the large amount of broken bonds at the ultimate state, which is discussed in Section 3.2.2.

It should be noted that, in the case of coating, there is a clear trend of increase in strength with the increase of carbonate content, as shown in Fig. 9(a). This behaviour is further associated with an improvement in dilatancy. On the other hand, there is negligible effect of carbonate content on the mechanical behaviour of pore filling type of samples, as shown in Fig. 9(b). This could be attributed to the relative low carbonate content (up to 3%) in the present study. This finding is in

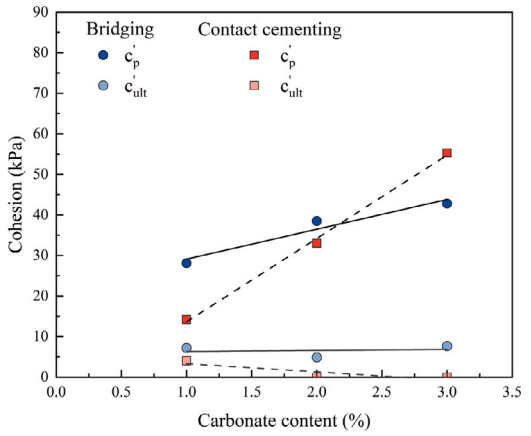

Fig. 8. Evolution of the cohesion at peak and ultimate states with carbonate content in the case of bridging and contact cementing.

agreement with what had been observed from DEM studies on pore-filling type of methane hydrate soils (Brugada et al., 2010; Ding et al., 2022, among others).

3.2. Microscopic observations

3.2.1. Coordination numbers

The coordination number Z can be used to describe granular assemblies and, in particular, the average number of contacts per particle. In

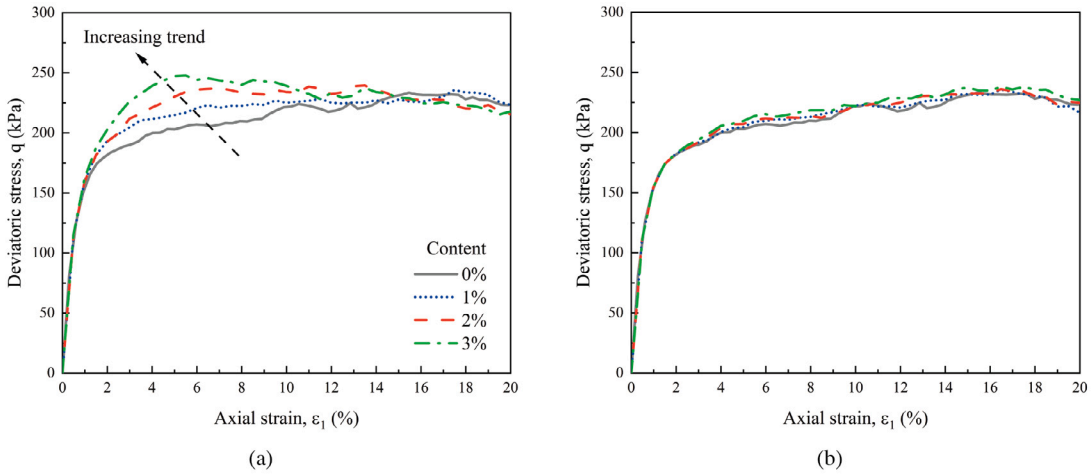

Fig. 9. Effects of carbonate content on the stress–strain response under a confining pressure of 100 kPa. Samples with (a) coating and (b) pore filling distribution patterns.

the case of structured polyphasic soils, the coordination number of the different (solid) phases provides better insights into the effects of the phases on the granular structure than the overall coordination number. The coordination number of phase Φ is defined as:

$$Z^{\Phi} = \frac{\sum_{i=1}^{N^{\Phi}} C_i}{N^{\Phi}} \tag{13}$$

where Φ represents either the sand (s) or carbonate (c) phase, C_i denotes the number of contacts that particle i (in phase Φ) has, and N^{Φ} is the number of particles in phase Φ of the assembly.

Fig. 10 presents the evolution of the coordination numbers of the sand and carbonate phases. Fig. 10(a) shows that cementation in the form of contact cementing increases drastically Z^s. This increase of Z^s is associated to the fact that each carbonate particle initially introduces two S–C contacts. In addition, for the same carbonate content (1%), the sample with contact cementing involves the largest number of carbonate particles (78765 for contact cementing, 7338 for bridging, 22893 for coating and 11448 for pore filling). Consequently, this distribution pattern leads to the highest Z^s among all cemented samples with a given carbonate content. Cementation in the form of bridging and coating also leads to a large increase in Z^s as carbonate particles connect to sand grains, which results in an increase in the number of contacts of sand grains. Z^s for the sample with pore filling evolves similarly to the uncemented sample. It drops initially and becomes stable at around 3 to 3.5. Note that this trend is generally observed in dense DEM samples (Rothenburg and Kruyt, 2004; Guo and Zhao, 2013). The similarity between Z^s in the cases of pore filling and the uncemented sample can be attributed to the negligible number of contacts introduced by carbonate particles to the sand grains. This can also be inferred from Fig. 10(b), which shows that Z^c of the sample with pore filling remains at a very low value close to 0, indicating that carbonate particles in the case of pore filling are basically not involved in the granular matrix. Z^c in the case of contact cementing starts at 4, as each carbonate particle initially connects to two sand grains and its two neighbouring carbonate particles. Similarly, Z^c in the cases of bridging and coating is initially equal to 2 and 1, respectively, as each carbonate particle connects respectively to two and one sand grains. Z^c in the cases of contact cementing and bridging gradually decreases during shearing due to the lost of sand–carbonate connections. On the other hand, Z^c in the case of coating shows a moderate increase as some of the carbonate particles gain new contacts with other particles during shearing.

The mechanical coordination number Z_m can further be used to describe the mechanical contribution of granular assemblies. Following Thornton (2000), the mechanical coordination number of phase Φ

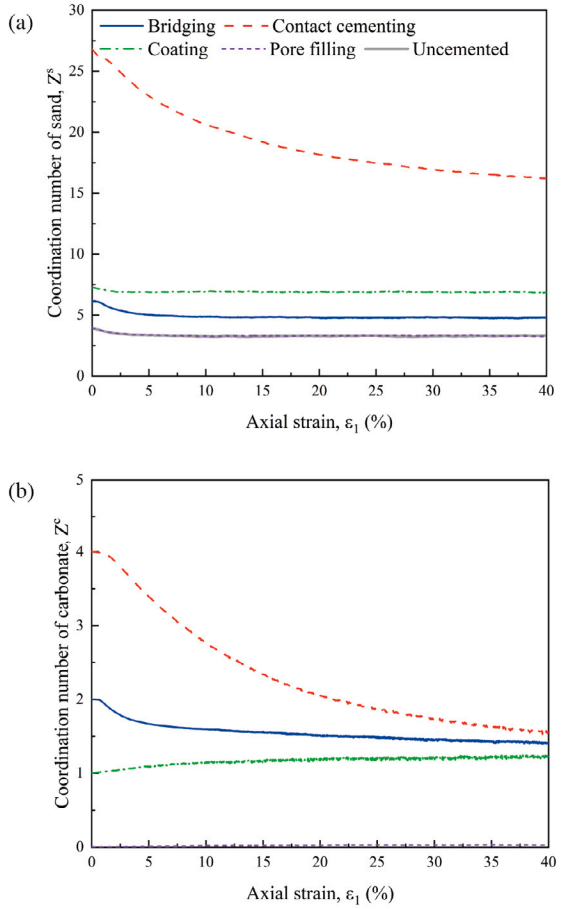

Fig. 10. Coordination numbers of the (a) sand and (b) carbonate phases for samples with 1% carbonate content and under a confining pressure of 100 kPa.

is defined in this study as:

$$Z_m^{\Phi} = \frac{\sum_{i=1}^{N^{\Phi}} C_i - N_1^{\Phi}}{N^{\Phi} - N_1^{\Phi} - N_0^{\Phi}} \tag{14}$$

where N_0^{Φ} is the number of particles in phase Φ without any contact and N_1^{Φ} is the number of particles in phase Φ with one contact only.

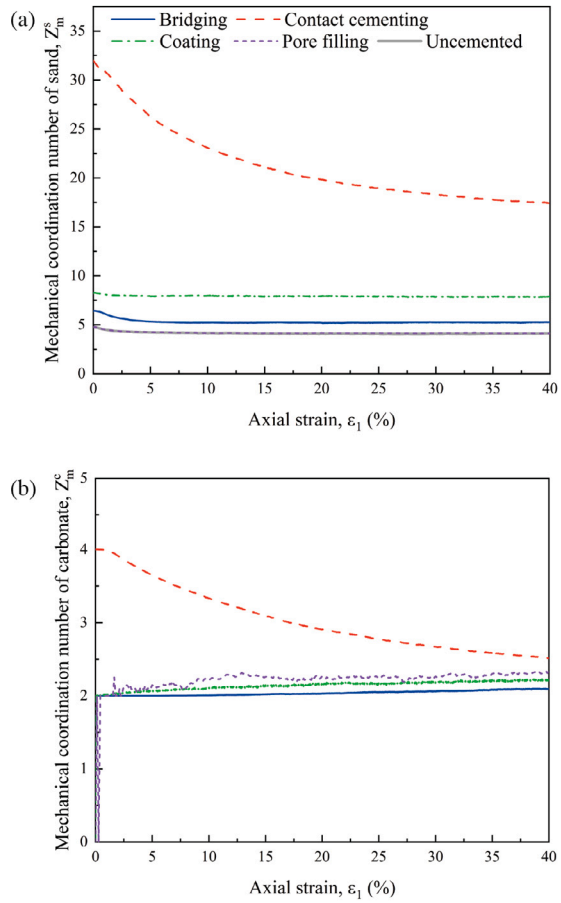

Fig. 11. Mechanical coordination numbers of the (a) sand and (b) carbonate phases for samples with 1% carbonate content and under a confining pressure of 100 kPa.

The mechanical coordination numbers for sand and carbonate are shown in Fig. 11. Z_m^s and Z^s exhibit similar trends for all types of samples. In contrast, Z_m^c evolves differently from Z^c in the cases of bridging, coating and pore filling. Z_m^c for the sample with a bridging carbonate distribution pattern almost keeps constant at 2. Z_m^c for the sample with carbonate coating starts from 0 and evolves around 2. In the case of pore filling, Z_m^c is initially equal to 0, increases rapidly at the beginning and goes above 2.

As discussed above, interesting insights can be obtained from the coordination number and mechanical coordination number. However, these numbers have limited capacity to explain the mechanical behaviour of bio-cemented soils upon shearing. In particular,

- The significant high values of Z^s and Z_m^s in the case of contact cementing hardly reflect the difference in mechanical response as compared to uncemented samples or bio-cemented samples displaying a different distribution pattern. Instead, samples with contact cementing show a lower peak strength than bridging samples (Fig. 4(a)). This inconsistency results from the fact that Z and Z_m are derived based on the number of contacts of every single particle, while several carbonate particles strengthen together one sand–sand contact in the case of contact cementing (Fig. 12). Therefore, an alternative approach for the definition of the coordination number for contact cementing case is to treat this set of carbonate particles as one equivalent bond.
- Samples with grain coating show the second highest Z^s and Z_m^s, while they do not exhibit obvious strength improvement. This suggests that it might be better to take into account only the contacts created by carbonate particles that bond sand grains.

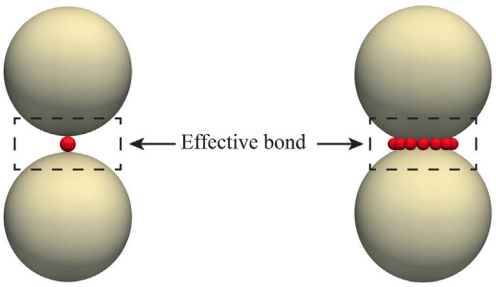

Fig. 12. Definition of effective bonds in samples with bridging (left) and contact cementing (right) carbonate distribution patterns.

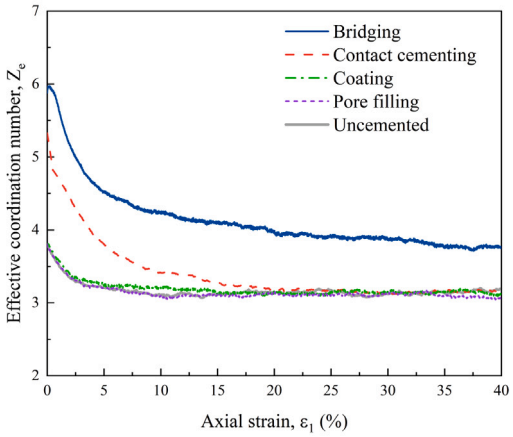

Fig. 13. Evolution of the effective coordination number upon shearing under a confining pressure of 100 kPa (carbonate content of the bio-cemented samples equal to 1%).

To reveal this feature, a new effective coordination number Z_e is introduced to describe the average number of effective bonds per sand grain. It is defined as:

$$Z_e = \frac{2\left(C_s + C_b\right)}{N_s} \tag{15}$$

where N_s is the number of sand particles, C_s is the total number of S–S contacts and C_b is the number of effective bonds in the cemented sample. As illustrated in Fig. 12, in the case of bridging, every carbonate particle initially connects two sand grains. Therefore, C_b is equal to the number of carbonate particles that have maintained their original two S–C contacts. In the case of contact cementing, several carbonate particles form a cement chain and, together, strengthen one S–S contact. Therefore, in this case, C_b is equal to the number of intact cement chains. Finally, in the case of coating and pore filling, C_b is equal to zero as carbonate particles do not introduce connections between sand grains.

Fig. 13 shows the evolution of the effective coordination number for different types of samples. It can be seen that the sample with cementation in the form of bridging shows initially the highest Z_e, followed by the sample with contact cementing. This indicates that new effective bonds are introduced in the case of bridging and contact cementing, leading to the improvement in strength (Fig. 4). Samples with a distribution of carbonate in the forms of coating and pore filling have almost the same coordination number as the uncemented sample, corresponding to no additional effective bonds introduced from carbonate particles.

3.2.2. Bond breakage behaviour

The stress–strain responses of samples with cementation in the forms of bridging and contact cementing are related to the evolution of

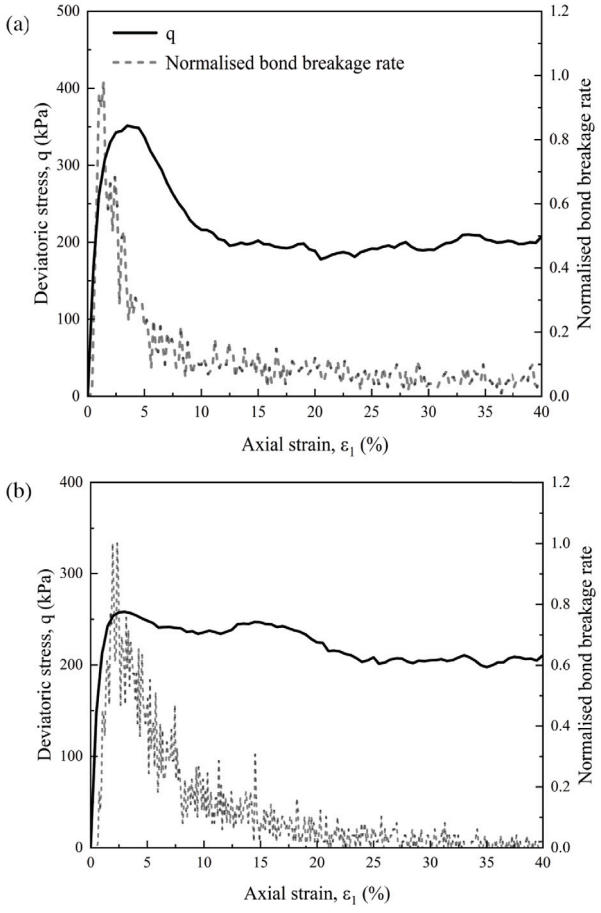

Fig. 14. Normalised bond breakage rate. Samples displaying (a) bridging and (b) contact cementing carbonate distribution patterns at 1% carbonate content and under a confining pressure of 100 kPa.

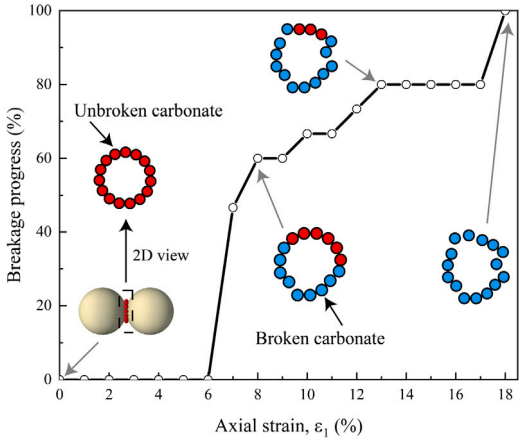

Fig. 15. Breakage progress of one cement chain. Data extracted from the sample with contact cementing and 1% carbonate content, sheared under a confining pressure of 100 kPa.

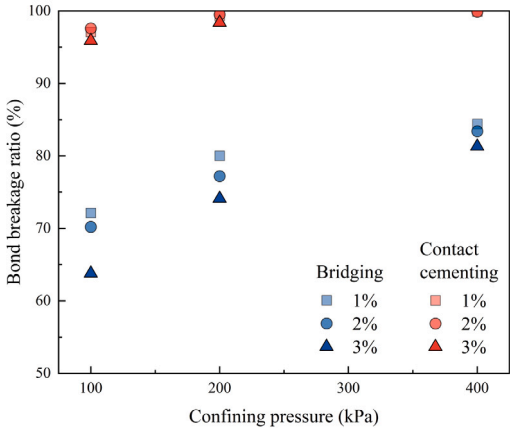

Fig. 16. Evolution of the bond breakage ratio at ε_1 = 40% with the confining pressure.

the microstructure upon shearing and, in particular, to the progressive breakage of bonds. The bond breakage ratio is defined as the ratio between the number of broken effective bonds and the number of initial bonds. Fig. 14 shows the evolution of the bond breakage rate (the derivative of the bond breakage ratio with respect to the axial strain) normalised by it maximum value in the corresponding simulation. Fig. 14(a) shows that, in the case of bridging, the maximum bond breakage rate occurs prior to the peak strength and coincides with the maximum tangent Young's modulus. It is followed by a sharp decrease. In that case, a single carbonate particle contributes to the contact between two sand grains. Accordingly, as soon as one of the initial S–C contacts is lost, the contribution to the strength improvement vanishes, leading to an overall softening. In the case of contact cementing (Fig. 14(b)), the post-peak behaviour is associated with a gradual decrease of the normalised bond breakage rate, leading to a progressive decrease in the overall strength and a more ductile behaviour as compared to the case of bridging. Fig. 15 shows the breakage progress of one cement chain monitored upon shearing. The breakage progress is described as the percentage of the number of carbonate particles which have lost any of their initial connections to a sand grain over the number of carbonate particles which have kept the original connections with the sand grain in that cement chain. The figure shows that the connections between sand grains and carbonate particles in the cement chain are not lost at the same time, but gradually at different strain levels.

The bond breakage ratio at the ultimate state is plotted in Fig. 16. The figure shows that, in the cases of both bridging and contact cementing, the ultimate bond breakage ratio increases with the confining pressure. In addition, most bonds are broken at the ultimate state in contact cementing cases, while the samples with a bridging pattern show a much lower bond breakage ratio as compared to contact cementing samples.

3.2.3. *Spatial distribution of breakage*

Fig. 17 presents the spatial distribution of breakage at an axial strain of 40% in the case of bridging and contact cementing under a confining pressure of 100 kPa. The black dots in Fig. 17 represent the carbonate particles which have lost any of their initial S–C contacts. It can be seen that for both bridging and contact cementing, the breakage events distribute uniformly among the sample, independently of the carbonate content. This finding is in agreement with observations on the lightly cemented sample by Li et al. (2017). However, strain localisation in the form of shear bands has been observed in bio-cemented sands by Lin et al. (2015), Montoya and DeJong (2015), Cui et al. (2017), Nafisi et al. (2019). The reason why shear localisation is not observed in this study may be attributed to the rigid walls used for the boundaries, which hamper the development of shear bands (Yang et al., 2019). Further DEM studies with soft membrane boundaries are necessary to assess the role of the boundary conditions on the development of strain localisation.

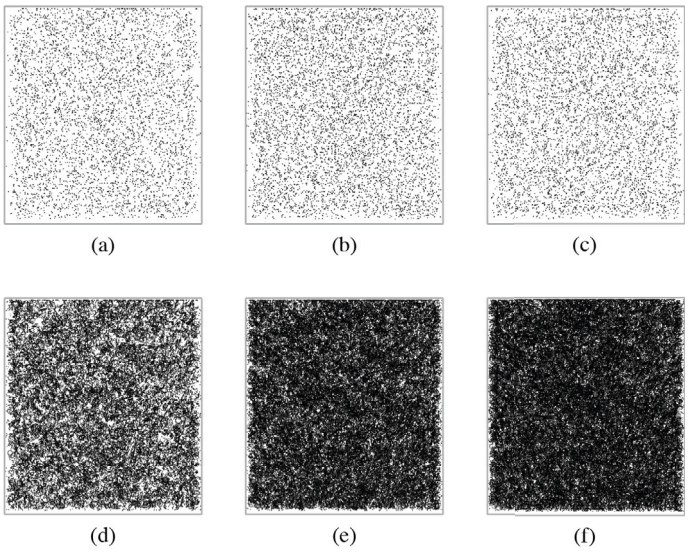

Fig. 17. Spatial distribution of breakage at an axial strain of 40%. (a) 1%, (b) 2% and (c) 3% carbonate content for samples with bridging carbonate particles, and (d) 1%, (e) 2% and (f) 3% carbonate content for samples with contact cementing.

4. Conclusions

In this paper, the complex microstructures of bio-cemented soils are simplified and idealised to focus on the main features of the carbonate distribution patterns. Four types of distribution patterns are investigated, namely bridging, contact cementing, grain coating and pore filling. Idealised bio-cemented samples which contain only one of the four distribution patterns are modelled in DEM. In each of the samples, carbonate particles are explicitly simulated with particles placed in designated positions to replicate the corresponding distribution pattern. The results from a series of drained triaxial compression simulations carried out in this paper show that the distribution patterns of carbonate strongly affect the mechanical behaviour of bio-cemented sands. While bridging and contact cementing lead to the highest improvement in stiffness, strength and dilatancy, coating shows a trend of improvement in strength with increasing carbonate content, associated with an increase in dilatancy. Bio-cemented samples displaying a pore filling pattern show a similar behaviour as uncemented samples. For a same carbonate content, cementation in the form of bridging leads to the largest strength improvement as well as the largest dilatancy enhancement, followed by contact cementing pattern. The strength parameters of bio-cemented soil samples are derived assuming a linear Mohr–Coulomb criterion. The formation of carbonate crystals in bridging pattern contributes to the shear resistance of bio-cemented soil by increasing both the friction angle and cohesion, while it mainly exhibits an increase in cohesion rather than friction angle for samples with contact cementing pattern. As some of the DEM parameters are not yet available from experiments, it is recommended, in future work, to carry out grain-scale micromechanical tests to provide references for DEM parameters and bridge the gap between DEM simulations and physical studies (see Wang et al., 2017; Kasyap et al., 2021; Ren et al., 2021; Reddy et al., 2022, among others). An engineering implication from the findings of the present paper is that to gain strength improvement the most effectively, treatment should ideally be tailored to precipitate calcium carbonate in bridging pattern. Therefore, further research on controlling the distribution pattern of the precipitated carbonate is needed.

CRediT authorship contribution statement

Aoxi Zhang: Methodology, Software, Investigation, Validation, Writing – original draft. **Anne-Catherine Dieudonné:** Conceptualization, Supervision, Writing – review & editing.

Declaration of competing interest

The authors declare that they have no known competing financial interests or personal relationships that could have appeared to influence the work reported in this paper.

Data availability

No data was used for the research described in the article.

Acknowledgements

The first author acknowledges support from the China Scholarship Council (CSC) and the Geo-Engineering Section of Delft University of Technology, The Netherlands. The authors would like to thank Dr. Beibing Dai, Dr. Jacques Desrues and Dr. Vanessa Magnanimo for the insightful discussions and advice on discrete element modelling.

References

Aboul Hosn, R., Sibille, L., Benahmed, N., Chareyre, B., 2017. Discrete numerical modeling of loose soil with spherical particles and interparticle rolling friction. Granul. Matter 19 (1), 1–12.

Al Qabany, A., Soga, K., 2013. Effect of chemical treatment used in MICP on engineering properties of cemented soils. Géotechnique 63 (4), 331–339.

Al Qabany, A., Soga, K., Santamarina, C., 2012. Factors affecting efficiency of microbially induced calcite precipitation. J. Geotech. Geoenviron. Eng. 138 (8), 992–1001.

Almajed, A., Tirkolaei, H.K., Kavazanjian, E., Hamdan, N., 2019. Enzyme induced biocementated sand with high strength at low carbonate content. Sci. Rep. 9 (1), 1135.

Bourrier, F., Kneib, F., Chareyre, B., Fourcaud, T., 2013. Discrete modeling of granular soils reinforcement by plant roots. Ecol. Eng. 61 (1), 646–657.

Brugada, J., Cheng, Y., Soga, K., Santamarina, J., 2010. Discrete element modelling of geomechanical behaviour of methane hydrate soils with pore-filling hydrate distribution. Granul. Matter 12 (5), 517–525.

Cheng, L., Cord-Ruwisch, R., Shahin, M.A., 2013. Cementation of sand soil by microbially induced calcite precipitation at various degrees of saturation. Can. Geotech. J. 50 (1), 81–90.
Cheng, L., Shahin, M.A., Chu, J., 2019. Soil bio-cementation using a new one-phase low-pH injection method. Acta Geotech. 14 (3), 615–626.
Cheng, L., Shahin, M.A., Mujah, D., 2016. Influence of key environmental conditions on microbially induced cementation for soil stabilization. J. Geotech. Geoenviron. Eng. 143 (1), 04016083.
Chu, J., Ivanov, V., Naeimi, M., Stabnikov, V., Liu, H.-L., 2014. Optimization of calcium-based bioclogging and biocementation of sand. Acta Geotech. 9 (2), 277–285.
Clarà Saracho, A., Haigh, S.K., Ehsan Jorat, M., 2021a. Flume study on the effects of microbial induced calcium carbonate precipitation (MICP) on the erosional behaviour of fine sand. Géotechnique 71 (12), 1135–1149.
Clarà Saracho, A., Lucherini, L., Hirsch, M., Peter, H.M., Terzis, D., Amstad, E., Laloui, L., 2021b. Controlling the calcium carbonate microstructure of engineered living building materials. J. Mater. Chem. A 9 (43), 24438–24451.
Cui, M.J., Zheng, J.-J., Zhang, R.J., Lai, H.J., Zhang, J., 2017. Influence of cementation level on the strength behaviour of bio-cemented sand. Acta Geotech. 12 (5), 971–986.
Cundall, P.A., Strack, O.D., 1979. A discrete numerical model for granular assemblies. Géotechnique 29 (1), 47–65.
Da Cruz, F., Emam, S., Prochnow, M., Roux, J.-N., Chevoir, F., 2005. Rheophysics of dense granular materials: Discrete simulation of plane shear flows. Phys. Rev. E 72 (2), 021309.
Dadda, A., Geindreau, C., Emeriault, F., Du Roscoat, S.R., Garandet, A., Sapin, L., Filet, A.E., 2017. Characterization of microstructural and physical properties changes in biocemented sand using 3D X-ray microtomography. Acta Geotech. 12 (5), 955–970.
Darby, K.M., Hernandez, G.L., DeJong, J.T., Boulanger, R.W., Gomez, M.G., Wilson, D.W., 2019. Centrifuge model testing of liquefaction mitigation via microbially induced calcite precipitation. J. Geotech. Geoenviron. Eng. 145 (10), 04019084.
DeJong, J.T., Mortensen, B.M., Martinez, B.C., Nelson, D.C., 2010. Bio-mediated soil improvement. Ecol. Eng. 36 (2), 197–210.
Ding, Y., Qian, A., Lu, H., Li, Y., Zhang, Y., 2022. DEM investigation of the effect of hydrate morphology on the mechanical properties of hydrate-bearing sands. Comput. Geotech. 143, 104603.
Ekprasert, J., Fongkaew, I., Chainakun, P., Kamngam, R., Boonsuan, W., 2020. Investigating mechanical properties and biocement application of CaCO3 precipitated by a newly-isolated lysinibacillus sp. WH using artificial neural networks. Sci. Rep. 10 (1), 1–13.
Evans, T., Khoubani, A., Montoya, B., 2014. Simulating mechanical response in bio-cemented sands. In: Computer Methods and Recent Advances in Geomechanics: Proceedings of the 14th International Conference of International Association for Computer Methods and Recent Advances in Geomechanics. Taylor & Francis Books Ltd, pp. 1569–1574.
Feng, K., Montoya, B., 2015. Influence of confinement and cementation level on the behavior of microbial-induced calcite precipitated sands under monotonic drained loading. J. Geotech. Geoenviron. Eng. 142 (1), 04015057.
Feng, K., Montoya, B., Evans, T., 2017. Discrete element method simulations of bio-cemented sands. Comput. Geotech. 85, 139–150.
Guo, N., Zhao, J., 2013. The signature of shear-induced anisotropy in granular media. Comput. Geotech. 47, 1–15.
Hamdan, N., Kavazanjian, E., 2016. Enzyme-induced carbonate mineral precipitation for fugitive dust control. Géotechnique 66 (7), 546–555.
Hoang, T., Alleman, J., Cetin, B., Ikuma, K., Choi, S.-G., 2018. Sand and silty-sand soil stabilization using bacterial enzyme–induced calcite precipitation (BEICP). Can. Geotech. J. 56 (6), 808–822.
Jiang, N.-J., Soga, K., 2017. The applicability of microbially induced calcite precipitation (MICP) for internal erosion control in gravel–sand mixtures. Géotechnique 67 (1), 42–55.
Jiang, M., Zhang, A., Li, T., 2019. Distinct element analysis of the microstructure evolution in granular soils under cyclic loading. Granul. Matter 21 (2), 1–16.
Kasyap, S., Senetakis, K., Coop, M.R., Zhao, J., 2021. Micromechanical behaviour in shearing of reproduced flat LBS grains with strong and weak artificial bonds. Acta Geotech. 16 (5), 1355–1376.
Khoubani, A., 2018. A New Bonding Model for the Particulate Simulation of Bio-Cemented Sand (with a Side Excursion on Percolation in Granular Mixtures) (Ph.D. thesis). Oregon State University.
Li, M., Cheng, X., Guo, H., 2013. Heavy metal removal by biomineralization of urease producing bacteria isolated from soil. Int. Biodeterioration Biodegrad. 76, 81–85.
Li, M., Cheng, X., Guo, H., Yang, Z., 2016. Biomineralization of carbonate by Terrabacter tumescens for heavy metal removal and biogrouting applications. J. Environ. Eng. 142 (9), C4015005.
Li, Z., Wang, Y., Ma, C., Mok, C., 2017. Experimental characterization and 3D DEM simulation of bond breakages in artificially cemented sands with different bond strengths when subjected to triaxial shearing. Acta Geotech. 12 (5), 987–1002.
Lin, H., Suleiman, M.T., Brown, D.G., Kavazanjian, E., 2015. Mechanical behavior of sands treated by microbially induced carbonate precipitation. J. Geotech. Geoenviron. Eng. 142 (2), 04015066.
Liu, L., Liu, H., Stuedlein, A.W., Evans, T.M., Xiao, Y., 2019. Strength, stiffness, and microstructure characteristics of biocemented calcareous sand. Can. Geotech. J. 56 (10), 1502–1513.
Mahawish, A., Bouazza, A., Gates, W.P., 2018. Improvement of coarse sand engineering properties by microbially induced calcite precipitation. Geomicrobiol. J. 35 (10), 887–897.
Montoya, B., DeJong, J., 2013. Healing of biologically induced cemented sands. Geotech. Lett. 3 (3), 147–151.
Montoya, B., DeJong, J., 2015. Stress-strain behavior of sands cemented by microbially induced calcite precipitation. J. Geotech. Geoenviron. Eng. 141 (6), 04015019.
Montoya, B., Feng, K., 2015. Deformation of microbial induced calcite bonded sands: A micro-scale investigation. In: Deformation Characteristics of Geomaterials. IOS Press, pp. 978–985.
Mujah, D., Shahin, M.A., Cheng, L., 2017. State-of-the-art review of biocementation by microbially induced calcite precipitation (MICP) for soil stabilization. Geomicrobiol. J. 34 (6), 524–537.
Nafisi, A., Montoya, B.M., Evans, T.M., 2020. Shear strength envelopes of biocemented sands with varying particle size and cementation level. J. Geotech. Geoenviron. Eng. 146 (3), 04020002.
Nafisi, A., Safavizadeh, S., Montoya, B.M., 2019. Influence of microbe and enzyme-induced treatments on cemented sand shear response. J. Geotech. Geoenviron. Eng. 145 (9), 06019008.
Okwadha, G.D., Li, J., 2010. Optimum conditions for microbial carbonate precipitation. Chemosphere 81 (9), 1143–1148.
Peng, Z., Redfern, S.A., 2013. Mechanical properties of quartz at the α-β phase transition: Implications for tectonic and seismic anomalies. Geochem. Geophys. Geosyst. 14 (1), 18–28.
Rakhimzhanova, A.K., Thornton, C., Minh, N.H., Fok, S.C., Zhao, Y., 2019. Numerical simulations of triaxial compression tests of cemented sandstone. Comput. Geotech. 113, 103068.
Reddy, N.S., He, H., Senetakis, K., 2022. DEM analysis of small and small-to-medium strain shear modulus of sands. Comput. Geotech. 141, 104518.
Ren, J., He, H., Senetakis, K., 2021. A micromechanical-based investigation on the frictional behaviour of artificially bonded analogue sedimentary rock with calcium carbonate. Pure Appl. Geophys. 178 (11), 4461–4486.
Rothenburg, L., Kruyt, N.P., 2004. Critical state and evolution of coordination number in simulated granular materials. Int. J. Solids Struct. 41 (21), 5763–5774.
Salifu, E., MacLachlan, E., Iyer, K.R., Knapp, C.W., Tarantino, A., 2016. Application of microbially induced calcite precipitation in erosion mitigation and stabilisation of sandy soil foreshore slopes: A preliminary investigation. Eng. Geol. 201, 96–105.
Shahin, M., Jamieson, K., Cheng, L., 2020. Microbial-induced carbonate precipitation for coastal erosion mitigation of sandy slopes. Géotech. Lett. 10 (2), 211–215.
Shen, Z., Jiang, M., Thornton, C., 2016. DEM simulation of bonded granular material. Part I: Contact model and application to cemented sand. Comput. Geotech. 75, 192–209.
Šmilauer, V., et al., 2015. Yade Documentation, second ed. The Yade Project, http://dx.doi.org/10.5281/zenodo.34073, http://yade-dem.org/doc/.
Tang, C.-S., Yin, L.-y., Jiang, N.-j., Zhu, C., Zeng, H., Li, H., Shi, B., 2020. Factors affecting the performance of microbial-induced carbonate precipitation (MICP) treated soil: A review. Environ. Earth Sci. 79 (5), 1–23.
Terzis, D., Laloui, L., 2018. 3-D micro-architecture and mechanical response of soil cemented via microbial-induced calcite precipitation. Sci. Rep. 8 (1), 1416.
Terzis, D., Laloui, L., 2019a. Cell-free soil bio-cementation with strength, dilatancy and fabric characterization. Acta Geotech. 14 (3), 639–656.
Terzis, D., Laloui, L., 2019b. A decade of progress and turning points in the understanding of bio-improved soils: A review. Geomech. Energy Environ. 19, 100116.
Thornton, C., 2000. Numerical simulations of deviatoric shear deformation of granular media. Géotechnique 50 (1), 43–53.
Utili, S., Nova, R., 2008. DEM analysis of bonded granular geomaterials. Int. J. Numer. Anal. Methods Geomech. 32 (17), 1997–2031.
Van Paassen, L.A., 2009. Biogrout, Ground Improvement by Microbial Induced Carbonate Precipitation (Ph.D. thesis). Delft University of Technology.
van Paassen, L.A., Ghose, R., van der Linden, T.J., van der Star, W.R., van Loosdrecht, M.C., 2010. Quantifying biomediated ground improvement by ureolysis: Large-scale biogrout experiment. J. Geotech. Geoenviron. Eng. 136 (12), 1721–1728.
Wang, Y., Konstantinou, C., Soga, K., Biscontin, G., Kabla, A.J., 2022. Use of microfluidic experiments to optimize MICP treatment protocols for effective strength enhancement of MICP-treated sandy soils. Acta Geotech. 1–22.
Wang, Y., Leung, S., 2008a. Characterization of cemented sand by experimental and numerical investigations. J. Geotech. Geoenviron. Eng. 134 (7), 992–1004.
Wang, Y.-H., Leung, S., 2008b. A particulate-scale investigation of cemented sand behavior. Can. Geotech. J. 45 (1), 29–44.
Wang, W., Nardelli, V., Coop, M.R., 2017. Micro-mechanical behaviour of artificially cemented sands under compression and shear. Géotech. Lett. 7 (3), 218–224.
Wu, S., Li, B., Chu, J., 2021. Stress-dilatancy behavior of MICP-treated sand. Int. J. Geomech. 21 (3), 04020264.
Xiao, P., Liu, H., Xiao, Y., Stuedlein, A.W., Evans, T.M., 2018. Liquefaction resistance of bio-cemented calcareous sand. Soil Dyn. Earthq. Eng. 107, 9–19.

Xiao, Y., Stuedlein, A.W., He, X., Han, F., Evans, T.M., Pan, Z., Lin, H., Chu, J., van Paassen, L., 2021a. Lateral responses of a model pile in biocemented sand. Int. J. Geomech. 21 (11), 06021027.

Xiao, Y., Wang, Y., Wang, S., Evans, T.M., Stuedlein, A.W., Chu, J., Zhao, C., Wu, H., Liu, H., 2021b. Homogeneity and mechanical behaviors of sands improved by a temperature-controlled one-phase MICP method. Acta Geotech. 16 (5), 1417–1427.

Yang, P., Kavazanjian, E., Neithalath, N., 2019. Particle-scale mechanisms in undrained triaxial compression of biocemented sands: Insights from 3D DEM simulations with flexible boundary. Int. J. Geomech. 19 (4), 04019009.

Yu, C., Wang, H., Zhou, A., Cai, X., Wu, Z., 2019. Experimental study on strength and microstructure of cemented soil with different suctions. J. Mater. Civ. Eng. 31 (6), 04019082.

Zeng, C., Veenis, Y., Hall, C.A., Young, E.S., van der Star, W.R., Zheng, J.J., van Paassen, L.A., 2021. Experimental and numerical analysis of a field trial application of microbially induced calcite precipitation for ground stabilization. J. Geotech. Geoenviron. Eng. 147 (7), 05021003.

Zhang, A., Dieudonné, A.C., 2023. Effects of carbonate distribution inhomogeneity on the improvement level of bio-cemented sands: A DEM study. In: Challenges and Innovations in Geomechanics. IACMAG 2022, In: Lecture Notes in Civil Engineering, vol. 288, pp. 554–561.